A Robust GPU-Accelerated Kernel Compensation Solver with Novel Discretization for Photonic Crystals in Pseudochiral Media*

Chenhao Jin[†] and Hehu Xie[‡]

Abstract This paper develops a robust solver for the Maxwell eigenproblem in 3D photonic crystals (PCs) with pseudochiral media. The solver employs the Kernel Compensation technique under the framework of Yee's scheme to eliminate null space and enable matrix-free, GPU-accelerated operations via 3D discrete Fourier transform (DFT). Furthermore, we propose a novel discretization for permittivity tensor containing off-diagonal entries and rigorously prove that the resulting matrix is Hermitian positive definite (HPD), which ensures the correctness of the kernel compensation technique. Numerical experiments on several benchmark examples are demonstrated to validate the robustness and accuracy of our scheme.

Keywords Maxwell eigenproblem; Photonic Crystals; Yee's scheme; Finite difference; Kernel compensation techique; Pseudochiral media; GPU Acceleration.

1 Introduction

Photonic crystals (PCs) are foundational to modern physics and engineering, offering unprecedented control over light propagation, which is vital for realizing devices like integrated lasers, efficient filters, and advanced optical transistors. The mathematical challenge lies in effectively solving the time-harmonic Maxwell's equations for dealing with null space and numerical accuracy. The governing system, defined in \mathbb{R}^3 , starts with:

$$\begin{cases} \nabla \times (\varepsilon^{-1} \nabla \times \mathbf{H}) = \omega^2 \mathbf{H}, & \text{in } \mathbb{R}^3, \\ \nabla \cdot \mathbf{H} = 0, & \text{in } \mathbb{R}^3. \end{cases}$$
 (1.1)

^{*}This work was supported by Strategic Priority Research Program of the Chinese Academy of Sciences (XDB0640000, XDB0640300, XDB0620203, XDA0480504), National Key Research and Development Program of China (2023YFB3309104), Natural Science Foundations of China (No. 1233000214), National Key Laboratory of Computational Physics (No. 6142A05230501), National Science Challenge Project (TZ2025007), National Center for Mathematics and Interdisciplinary Science, CAS.

[†]School of Mathematical Sciences, University of Science and Technology of China, Hefei, Anhui 230026, China. E-mail: kanit@mail.ustc.edu.cn

[‡]SKLMS, Academy of Mathematics and Systems Science, Chinese Academy of Sciences, No.55, Zhongguancun Donglu, Beijing 100190, China, and School of Mathematical Sciences, University of Chinese Academy of Sciences, Beijing, 100049, China. E-mail: hhxie@lsec.cc.ac.cn

This magnetic field formulation is advantageous for numerical discretization, particularly concerning our kernel compensation techniques aimed at eliminating the null space.

According to Bloch's theorem, H satisfies the quasi-periodic condition

$$H(x + a_i) = e^{i\mathbf{k}\cdot\mathbf{a}_i}H(x), \quad i = 1, 2, 3,$$
(1.2)

where $\mathbf{k} = (\mathbf{k}_1, \mathbf{k}_2, \mathbf{k}_3) \in \mathbb{R}^3$ is the wave number vector located in the first Brillouin zone, $\{a_i\}_{i=1}^3$ are lattice translation vectors that span the primitive cell

$$\Omega := \left\{ \boldsymbol{x} \in \mathbb{R}^3 : \boldsymbol{x} = \sum_{i=1}^3 x_i \boldsymbol{a}_i, \ x_i \in [0, 1], \ i = 1, 2, 3 \right\}.$$
(1.3)

One can find detailed definitions of a_i and k in (4.1), (4.2) in Section 4. We introduce the transformation $H_k(x) := e^{-i\mathbf{k}\cdot x}H(x)$ to convert the problem into one with pure periodic boundary conditions. This approach, which involves the shifted Nabla operator $\nabla_k := \nabla + i\mathbf{k}I$, yields the shifted system with periodic boundary condition. To avoid ambiguity of notation the subscript \mathbf{k} of H_k is left out. We keep using \mathbf{H} to refer to magnetic field and the variants of (1.1) hereafter:

$$\begin{cases}
\nabla_{\mathbf{k}} \times (\varepsilon^{-1} \nabla_{\mathbf{k}} \times \mathbf{H}) = \omega^{2} \mathbf{H}, & \text{in } \Omega, \\
\nabla_{\mathbf{k}} \cdot \mathbf{H} = 0, & \text{in } \Omega, \\
\mathbf{H}(\mathbf{x} + \mathbf{a}_{i}) = \mathbf{H}(\mathbf{x}), & i = 1, 2, 3.
\end{cases}$$
(1.4)

This transformation is common in variational approaches [13] but is particularly advantageous for finite difference schemes, as it imparts a simpler cyclic structure to the discrete system—an attribute crucial for efficient matrix-free operations here.

The inverse permittivity ε^{-1} is piecewise constant and defined by

$$\varepsilon^{-1}(\boldsymbol{x}) = \begin{cases} \varepsilon_1, & \boldsymbol{x} \in \Omega_1, \\ I_3, & \boldsymbol{x} \in \Omega_0 := \Omega \backslash \Omega_1, \end{cases}$$
 (1.5)

where ε_1 is a 3 × 3 Hermitian positive definite (HPD) matrix. When ε_1 is a scalar matrix, the system (1.4) is referred to as isotropic; when ε_1 contains nonzero off-diagonal entries, (1.4) is called a pseudochiral system.

Numerical solution of such systems presents two essential challenges. The first is the null space of the continuous curl operator, addressed by our prior work [7]. The second, our present focus, is the discretization of the pseudochiral permittivity tensor ε , for which a direct finite-difference-based approach does not exist. We design a novel dicretization for the ε^{-1} in (1.5) where nonzero entries of ε_1 occur. Although finite element methods [2, 3, 12] and plane wave expansion methods [4, 16] are alternative options, they yield a generalized eigenvalue problem. The finite difference framework [5, 6] is highly attractive as it produces a simpler eigenvalue problem and benefits from a circulant matrix structure. Furthermore, we impose a coordinate transform on the boundary condition in (1.4) that aligns periodicity with the standard \mathbb{R}^3 basis. Such treatment also yields highly efficient GPU acceleration.

In this paper, we overcome the limitations solving the pseudochiral system with finite difference method and present a corresponding robust, efficient eigensolver built upon the kernel compensation technique. We summarize the key innovations as follows:

- We complete the theoretical foundation of the kernel compensation technique by rigorously demonstrating the exact structure of the null space and how the penalized coefficient should be chosen. Such technique allows matrix-free operations that reduce the per-iteration cost to a single global 3D discrete Fourier transform (DFT).
- We propose an innovative discretization concerning permittivity ε of the pseudochiral system, strictly proving that the corresponding discrete matrix is HPD under physical constraints. This HPD property is essential for ensuring the correctness of the Kernel Compensation technique.
- We present extensive numerical computations on various pseudochiral systems and implement GPU acceleration of the entire code for high-performance large-scale simulations.

The paper is outlined as follows. Section 2 formally introduces the core discretization and the kernel compensation formulation. Section 3 details our innovative treatment of the anisotropic permittivity tensor and establishes the theoretical proof of the HPD property. Section 4 presents extensive numerical experiments, including band structure analysis and computational performance benchmarks. We conclude in Section 5.

2 Discretization and Kernel Compensation

In Subsection 2.1, we present Yee's scheme [17] to discretize Maxwell's equation with shifted nabla operator. Matrix representations of discrete differential operators are also provided. The results are generalized to arbitrary lattices $\{a_i\}_{i=1}^3$ through coordinate transform, which is covered in Subsection 2.2. We then discuss the kernel compensation technique that eliminates the null space in Subsection 2.3. In Subsection 2.4, we seek matrix-free operations of sparse matrix-vector multiplication and design an efficient preconditioner.

2.1 Yee's Scheme

In this subsection, we set the primitive lattice vectors to be the standard orthonormal basis of \mathbb{R}^3 , i.e., $\mathbf{a}_i = \mathbf{e}_i$ and $\Omega = (0,1)^3$. We uniformly partition the domain Ω into a cubic grid with division $N \in \mathbb{N}^*$, grid size h = 1/N in each x, y, z direction. Although the generalization to distinct divisions along each axis is straightforward, it does not yield improvements. The distributions of node, edge, face and volume DoFs are shown in Figure 1.

In Yee's staggered grid the magnetic field $\mathbf{H} = (H_1, H_2, H_3)$ is approximated by face DoFs, while electric field $\mathbf{E} = (E_1, E_2, E_3)$ by edge DoFs:

$$\mathbf{E} \mapsto \mathbf{E}_{h} := (\mathbf{E}_{h}^{1}, \ \mathbf{E}_{h}^{2}, \ \mathbf{E}_{h}^{3})^{\top} := (E_{i-\frac{1}{2},j,k}^{1}, \ E_{i,j-\frac{1}{2},k}^{2}, \ E_{i,j,k-\frac{1}{2}}^{3})^{\top},
\mathbf{H} \mapsto \mathbf{H}_{h} := (\mathbf{H}_{h}^{1}, \ \mathbf{H}_{h}^{2}, \ \mathbf{H}_{h}^{3})^{\top} := (H_{i,j-\frac{1}{2},k-\frac{1}{2}}^{1}, \ H_{i-\frac{1}{2},j,k-\frac{1}{2}}^{2}, \ H_{i-\frac{1}{2},j-\frac{1}{2},k}^{3})^{\top},$$
(2.1)

where $1 \leq i, j, k \leq N$. Subscripts represent discrete coordinates on the Cartesian grid where the function is evaluated. The image of the divergence operator $\nabla_{\mathbf{k}}$ acting on an arbitrary

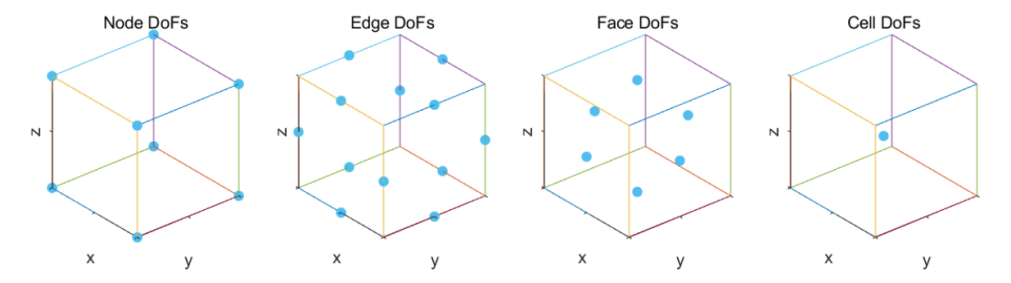


Figure 1: DoFs of scalar and vector grid functions on a single cell

periodic scalar function ψ , for example, is approximated by volume DoFs:

$$\psi \mapsto \psi_h := \left(\psi_{i-\frac{1}{2}, j-\frac{1}{2}, k-\frac{1}{2}}\right).$$
 (2.2)

Therefore we introduce discrete spaces of edge, face and volume DoFs as

$$\mathcal{E}_{h} := \left\{ \left(E_{i-\frac{1}{2},j,k}^{1}, \quad E_{i,j-\frac{1}{2},k}^{2}, \quad E_{i,j,k-\frac{1}{2}}^{3} \right) : \boldsymbol{E} \text{ is a periodic field on } \Omega \right\} \simeq \mathbb{C}^{3N^{3}},$$

$$\mathcal{F}_{h} := \left\{ \left(H_{i,j-\frac{1}{2},k-\frac{1}{2}}^{1}, \quad H_{i-\frac{1}{2},j,k-\frac{1}{2}}^{2}, \quad H_{i-\frac{1}{2},j-\frac{1}{2},k}^{3} \right) : \boldsymbol{H} \text{ is a periodic field on } \Omega \right\} \simeq \mathbb{C}^{3N^{3}}, \quad (2.3)$$

$$\mathcal{V}_{h} := \left\{ \left(\psi_{i-\frac{1}{2},j-\frac{1}{2},k-\frac{1}{2}} \right) : \psi \text{ is a periodic scalar function on } \Omega \right\} \simeq \mathbb{C}^{N^{3}}.$$

In the double curl problem (1.4), the discrete outer curl operator maps edge DoFs to face DoFs. Crucially, the inner curl operator is derived as the adjoint of the outer operator, mapping face DoFs to edge DoFs. We denote the matrix representations for the outer curl operator $\nabla_{\mathbf{k}} \times$, the permittivity ε and the divergence operator $\nabla_{\mathbf{k}} \cdot$ as \mathcal{A} , $\mathcal{M}_{\varepsilon}$, \mathcal{B} , respectively. Then due to the adjoint relation [7, 10], matrix representation of the inner curl operator $\nabla_{\mathbf{k}} \times$ is simply \mathcal{A}^{\dagger} , where "†" denotes the conjugate transpose. We have

$$\mathcal{A}: \mathcal{E}_h \to \mathcal{F}_h, \quad \mathcal{M}_{\varepsilon}: \mathcal{E}_h \to \mathcal{E}_h, \quad \mathcal{A}^{\dagger}: \mathcal{F}_h \to \mathcal{E}_h, \quad \mathcal{B}: \mathcal{F}_h \to \mathcal{V}_h.$$
 (2.4)

For any $E_h \in \mathcal{E}_h$, the image AE_h along each axis has the following expressions:

$$(\mathcal{A}\boldsymbol{E}_{h})_{i,j-\frac{1}{2},k-\frac{1}{2}} \ = \ \frac{E_{i,j,k-\frac{1}{2}}^{3} - E_{i,j-1,k-\frac{1}{2}}^{3}}{h} - \frac{E_{i,j-\frac{1}{2},k}^{2} - E_{i,j-\frac{1}{2},k-1}^{2}}{h} \\ + \mathrm{i} \left(k_{2} \frac{E_{i,j-1,k-\frac{1}{2}}^{3} + E_{i,j,k-\frac{1}{2}}^{3}}{2} - k_{3} \frac{E_{i,j-\frac{1}{2},k-1}^{2} + E_{i,j-\frac{1}{2},k}^{2}}{2} \right),$$

$$(\mathcal{A}\boldsymbol{E}_{h})_{i-\frac{1}{2},j,k-\frac{1}{2}} \ = \ \frac{E_{i-\frac{1}{2},j,k}^{1} - E_{i-\frac{1}{2},j,k-1}^{1}}{h} - \frac{E_{i,j,k-\frac{1}{2}}^{3} - E_{i-1,j,k-\frac{1}{2}}^{3}}{h} \\ + \mathrm{i} \left(k_{3} \frac{E_{i-\frac{1}{2},j,k-1}^{1} + E_{i-\frac{1}{2},j,k}^{1}}{2} - k_{1} \frac{E_{i-1,j,k-\frac{1}{2}}^{3} - E_{i,j,k-\frac{1}{2}}^{3}}{2} \right),$$

$$(\mathcal{A}\boldsymbol{E}_{h})_{i-\frac{1}{2},j-\frac{1}{2},k} \ = \ \frac{E_{i,j-\frac{1}{2},k}^{2} - E_{i-1,j-\frac{1}{2},k}^{2}}{h} - \frac{E_{i-\frac{1}{2},j,k}^{1} - E_{i-\frac{1}{2},j-1,k}^{1}}{h}$$

$$+\mathrm{i}\left(\mathrm{k}_{1}\frac{E_{i-1,j-\frac{1}{2},k}^{2}+E_{i,j-\frac{1}{2},k}^{2}}{2}-\mathrm{k}_{2}\frac{E_{i-\frac{1}{2},j-1,k}^{1}+E_{i-\frac{1}{2},j,k}^{1}}{2}\right).$$

Likewise, for any $H_h \in \mathcal{F}_h$, the discrete divergence is formulated by

$$(\mathcal{B}\boldsymbol{H}_{h})_{i-\frac{1}{2},j-\frac{1}{2},k-\frac{1}{2}} = \frac{H_{i,j-\frac{1}{2},k-\frac{1}{2}}^{1} - H_{i-1,j-\frac{1}{2},k-\frac{1}{2}}^{1}}{h} + \frac{H_{i-\frac{1}{2},j,k-\frac{1}{2}}^{2} - H_{i-\frac{1}{2},j-1,k-\frac{1}{2}}^{2}}{h} + \frac{H_{i-\frac{1}{2},j-\frac{1}{2},k-\frac{1}{2}}^{3} - H_{i-\frac{1}{2},j-\frac{1}{2},k-\frac{1}{2}}^{3}}{h} + i\left(k_{1}\frac{H_{i-1,j-\frac{1}{2},k-\frac{1}{2}}^{1} + H_{i,j-\frac{1}{2},k-\frac{1}{2}}^{1}}{2} + k_{2}\frac{H_{i-\frac{1}{2},j-1,k-\frac{1}{2}}^{2} + H_{i-\frac{1}{2},j,k-\frac{1}{2}}^{3}}{2} + k_{3}\frac{H_{i-\frac{1}{2},j-\frac{1}{2},k-1}^{3} + H_{i-\frac{1}{2},j-\frac{1}{2},k}^{3}}{2}\right).$$

The notations of E_h , H_h are adopted from (2.3). We may formulate the explicit matrix representations through circulant matrix below:

$$\mathbf{D}_{1} := \frac{1}{h} \begin{pmatrix} 1 & & & -1 \\ -1 & 1 & & & \\ & & \ddots & & \\ & & -1 & 1 \end{pmatrix} \in \mathbb{R}^{N \times N}, \quad \mathbf{D}_{0} := \frac{1}{2} \begin{pmatrix} 1 & & & 1 \\ 1 & 1 & & & \\ & & \ddots & & \\ & & 1 & 1 \end{pmatrix} \in \mathbb{R}^{N \times N}.$$
 (2.5)

Then directional derivatives combined with actions of \mathbf{k} can be represented by the following matrix blocks using Kronecker product \otimes (I_N denotes the identity matrix of dimension N):

$$\mathcal{D}_{i} = \mathcal{D}_{1,i} + ik_{i}\mathcal{D}_{0,i} \quad i = 1, 2, 3, \text{ where}$$

$$\mathcal{D}_{s,1} = I_{N^{2}} \otimes \mathbf{D}_{s}, \quad \mathcal{D}_{s,2} = I_{N} \otimes \mathbf{D}_{s} \otimes I_{N}, \quad \mathcal{D}_{s,3} = \mathbf{D}_{s} \otimes I_{N^{2}}, \quad s = 1, 2.$$

$$(2.6)$$

Therefore the matrix representations of \mathcal{A} , \mathcal{B} are given by

$$\mathcal{A} = \begin{pmatrix}
-\mathcal{D}_3 & \mathcal{D}_2 \\
\mathcal{D}_3 & -\mathcal{D}_1 \\
-\mathcal{D}_2 & \mathcal{D}_1
\end{pmatrix}, \quad \mathcal{B} = \begin{pmatrix}
\mathcal{D}_1 & \mathcal{D}_2 & \mathcal{D}_3
\end{pmatrix}.$$
(2.7)

The assembling of the discrete permittivity matrix $\mathcal{M}_{\varepsilon}$ will be covered in Section 3. In the rest of this section we assume that $\mathcal{M}_{\varepsilon}$ is HPD.

2.2 Coordinate Transform

In Subsection 2.1, the periodic cell Ω is assumed to be a unit cube. For general cases, the formulations (2.6) and (2.7) can be generalized for any linearly independent lattice vectors $\{a_i\}_{i=1}^3$ through a simple coordinate transform. If we apply the following operation:

Replace
$$\boldsymbol{H}$$
 in (1.4) by $(\boldsymbol{x} \mapsto \boldsymbol{H}(\mathbf{A}\boldsymbol{x}))$, $\mathbf{A} = (\boldsymbol{a}_1, \boldsymbol{a}_2, \boldsymbol{a}_3)$, (2.8)

then equation (1.4) can be equivalently written as

$$\begin{cases}
\nabla_{\mathbf{A},\mathbf{k}} \times \varepsilon^{-1} \nabla_{\mathbf{A},\mathbf{k}} \times \boldsymbol{H} = \omega^{2} \boldsymbol{H}, & \text{in } (0,1)^{3}, \\
\nabla_{\mathbf{A},\mathbf{k}} \cdot \boldsymbol{H} = 0, & \text{in } (0,1)^{3}, \\
\boldsymbol{H}(\boldsymbol{x} + \boldsymbol{e}_{i}) = H(\boldsymbol{x}), & i = 1, 2, 3,
\end{cases}$$
(2.9)

where $\nabla_{\mathbf{A},\mathbf{k}} = \nabla_{\mathbf{A}} + i\mathbf{k}I$ and $\nabla_{\mathbf{A}}$ is given by

$$\nabla_{\mathbf{A}} = \left(\sum_{j=1}^{3} b_{j1} \frac{\partial}{\partial x_{j}}, \sum_{j=1}^{3} b_{j2} \frac{\partial}{\partial x_{j}}, \sum_{j=1}^{3} b_{j3} \frac{\partial}{\partial x_{j}}\right)^{\top}, \quad b_{ij} = (\mathbf{A}^{-1})_{ij}.$$
 (2.10)

In this case we reformulate the matrix blocks in (2.6) as:

$$\hat{\mathcal{D}}_i = \sum_{j=1}^3 b_{ji} \mathcal{D}_{1,i} + i k_i \mathcal{D}_{0,i}, \quad i = 1, 2, 3.$$
(2.11)

The matrix \mathcal{A}, \mathcal{B} preserves the structure in (2.7) by updating matrix blocks $\hat{\mathcal{D}}_i$. In summary, the discrete formulation of model problem (1.4) as well as (2.9) results in the system:

$$\begin{cases}
\left(\mathcal{A}\mathcal{M}_{\varepsilon}\mathcal{A}^{\dagger}\right)\boldsymbol{H}_{h} = \omega_{h}^{2}\boldsymbol{H}_{h}, \\
\mathcal{B}\boldsymbol{H}_{h} = \mathbf{0}.
\end{cases} (2.12)$$

2.3 Kernel Compensation

Kernel compensation is introduced to find the nontrivial eigenpairs that satisfy the discrete divergence-free condition $\mathcal{B}\mathbf{H}_h = 0$ while avoiding the null space of \mathcal{A}^{\dagger} , which is formulated as:

The first several smallest positive eigenvalues of
$$(\mathcal{A}\mathcal{M}_{\varepsilon}\mathcal{A}^{\dagger} + \gamma\mathcal{B}^{\dagger}\mathcal{B})\boldsymbol{H}_{h} = \omega_{h}^{2}\boldsymbol{H}_{h}$$
 (2.13) coincide with (2.12) when $\gamma > 0$ is sufficiently large.

Now, we come to prove the correctness of (2.13) with an explicit choice of the penalty coefficient γ . For this aim, we first introduce the following lemma.

Lemma 2.1. If $\mathbf{C} \in \mathbb{C}^{N \times N}$ is a circulant matrix with the first row (c_1, \dots, c_N) , then it can be diagonalized by the unitary DFT matrix \mathbf{F} as

$$\mathbf{C} = \mathbf{F} \operatorname{diag}(\lambda_1, \dots, \lambda_N) \mathbf{F}^{\dagger}, \quad \lambda_i = \sum_{j=1}^{N} c_j \omega^{(i-1)(j-1)}, \quad i = 1, \dots, N.$$
 (2.14)

The matrix $\mathbf{F} = (F_{ij})_{1 \leq i,j \leq N}$ is defined by $F_{ij} = \frac{1}{\sqrt{N}} \omega^{(i-1)(j-1)}$ and $\omega = \exp(i\frac{2\pi}{N})$. As a corollary, the product of any two circulant matrices is commutative: $\mathbf{C}_1\mathbf{C}_2 = \mathbf{C}_2\mathbf{C}_1$ whenever $\mathbf{C}_1, \mathbf{C}_2$ are circulant matrices.

Proof. The proof is provided in
$$[1]$$
.

Proposition 2.2. The matrices A, B defined in (2.6), (2.7) and (2.11) satisfy: BA = 0.

Proof. It suffices to verify that $\hat{\mathcal{D}}_i\hat{\mathcal{D}}_j = \hat{\mathcal{D}}_j\hat{\mathcal{D}}_i$, which is equivalent to the commutativity of the product of $\mathcal{D}_{s,i}$ and $\mathcal{D}_{t,j}$ for any $s,t \in \{1,2\}$ and $i,j \in \{1,2,3\}$. When $i \neq j$ the result is proved by the mixed product property

$$(A_1 \otimes B_1)(A_2 \otimes B_2) = (A_1 A_2) \otimes (B_1 B_2) \tag{2.15}$$

for any A_i , B_i with compatible shapes. Thus multiplications of $\mathcal{D}_{s,i}$ and $\mathcal{D}_{t,i}$ are commutative. When i = j the result holds due to Lemma 2.1 and the mixed product property (2.15).

Proposition 2.3 (Main Result of Kernel Compensation). For arbitrary matrices $\mathcal{A}, \mathcal{M}, \mathcal{B}, \mathcal{A}, \mathcal{M} \in \mathbb{C}^{N^{\mathcal{A}} \times N^{\mathcal{A}}}$ and $\mathcal{B} \in \mathbb{C}^{N^{\mathcal{B}} \times N^{\mathcal{A}}}$, are such that $\mathcal{B}\mathcal{A} = \mathbf{0}$, \mathcal{M} is HPD. We assume that

eigenvalues of
$$\mathcal{AMA}^{\dagger}$$
: $0, 0, \dots, 0 < \lambda_{1}^{\mathcal{A}} \leq \lambda_{2}^{\mathcal{A}} \leq \dots \leq \lambda_{N_{1}^{\mathcal{A}}}^{\mathcal{A}}$, (2.16)
eigenvalues of $\mathcal{B}^{\dagger}\mathcal{B}$: $0, 0, \dots, 0 < \lambda_{1}^{\mathcal{B}} \leq \lambda_{2}^{\mathcal{B}} \leq \dots \leq \lambda_{N_{1}^{\mathcal{B}}}^{\mathcal{B}}$.

Then the eigenvalue distributions of $\mathcal{AMA}^{\dagger} + \gamma \mathcal{B}^{\dagger} \mathcal{B}$ are

$$\underbrace{0, \cdots, 0}_{\text{optimal energy of } 0} < \lambda_1 \le \lambda_2 \le \cdots \le \lambda_m \le \cdots,$$
(2.17)

where γ is an arbitrary positive number, $\mathcal{H} := \ker \mathcal{A}^{\dagger} \cap \ker \mathcal{B}$. There holds

$$\{\lambda_1, \cdots, \lambda_m, \cdots\} = \{\lambda_1^{\mathcal{A}}, \cdots, \lambda_{N_{\mathcal{A}}^{\mathcal{A}}}^{\mathcal{A}}\} \cup \{\gamma \lambda_1^{\mathcal{B}}, \cdots, \gamma \lambda_{N_{\mathcal{B}}^{\mathcal{B}}}^{\mathcal{B}}\}.$$
 (2.18)

Proof. We refer the reader to [7] for the proof.

The kernel compensation formulation (2.13) allows us to recover the nonzero eigenvalues of $\mathcal{AM}_{\varepsilon}\mathcal{A}^{\dagger}$ by computing the spectrum of the penalized system $\mathcal{AM}_{\varepsilon}\mathcal{A}^{\dagger} + \gamma \mathcal{B}^{\dagger}\mathcal{B}$. Proposition 2.3 shows the first m smallest positive eigenvalues of the two systems are identical, provided that γ satisfies $\gamma \lambda_1^{\mathcal{B}} \geq \lambda_m^{\mathcal{A}}$. To characterize the resulting null space \mathcal{H} and determine an appropriate value for the penalty coefficient γ , we present the following analysis.

Lemma 2.4. When the coordinate change (2.8) $\mathbf{A} = I_3$, we have

(1). The block matrices \mathcal{A} and \mathcal{B} satisfy $\mathcal{A}\mathcal{A}^{\dagger} + \mathcal{B}^{\dagger}\mathcal{B} = \operatorname{diag}(\mathcal{L}, \mathcal{L}, \mathcal{L})$ with

$$\mathcal{L} = \mathcal{B}\mathcal{B}^{\dagger} = \mathcal{D}_1^{\dagger} \mathcal{D}_1 + \mathcal{D}_2^{\dagger} \mathcal{D}_2 + \mathcal{D}_3^{\dagger} \mathcal{D}_3 \in \mathbb{C}^{N^3 \times N^3}, \tag{2.19}$$

(2). If there holds conditions

$$\mathbf{k} \neq \mathbf{0}, \quad \max_{i=1,2,3} |\mathbf{k}_i| \le \pi, \quad grid \ size \ h = \frac{1}{N} < \frac{1}{\pi}, \tag{2.20}$$

then the smallest nonzero eigenvalue of $\mathcal{B}^{\dagger}\mathcal{B}$, as is denoted by $\lambda_1^{\mathcal{B}}$ in Proposition 2.3, satisfies $\lambda_1^{\mathcal{B}} = \lambda_{\min}(\mathcal{L}) = \|\mathbf{k}\|_2^2$.

Proof. A direct computation of $\mathcal{A}\mathcal{A}^{\dagger} + \mathcal{B}^{\dagger}\mathcal{B}$ yields a block diagonal matrix, provided that $\mathcal{D}_{i}^{\dagger}\mathcal{D}_{j} = \mathcal{D}_{j}\mathcal{D}_{i}^{\dagger}$ for $i \neq j$. This commutativity is guaranteed by the mixed product property of Kronecker products (2.15). The identity $\mathcal{D}_{i}^{\dagger}\mathcal{D}_{i} = \mathcal{D}_{i}\mathcal{D}_{i}^{\dagger}$ holds because $\mathbf{K}_{i} := \mathbf{D}_{1} + \mathrm{ik}_{i}\mathbf{D}_{0}$ is a circulant matrix and thus normal, so is each block \mathcal{D}_{i} ; We establish (2.19).

To prove (2), since $\mathcal{B}^{\dagger}\mathcal{B}$ shares the same nonzero eigenvalues with $\mathcal{L} = \mathcal{B}\mathcal{B}^{\dagger}$, we analyze the spectrum of \mathcal{L} . The matrix $\mathbf{K}_{i}^{\dagger}\mathbf{K}_{i}$ is circulant, and by setting $c_{i} = \frac{1}{h} + i\frac{\mathbf{k}_{i}}{2}$, its first row is $(2|c_{i}|^{2}, -c_{i}^{2}, \cdots, -\overline{c_{i}}^{2})$. Applying Lemma 2.1, its eigenvalues are

$$\mu_j^{(i)} := \lambda_j(\mathbf{K}_i^{\dagger} \mathbf{K}_i) = 2\left(|c_i|^2 - \text{re}(c_i^2 \omega^j)\right) = \left(\frac{2}{h^2} + \frac{\mathbf{k}_i^2}{2}\right) \left(1 - \cos(\phi_i + 2j\pi h)\right),\tag{2.21}$$

for $j = 1, \dots, N$ and $\tan \phi_i = \frac{4\mathbf{k}_i h}{4 - \mathbf{k}_i^2 h^2}$. The spectrum of $\mathcal{L} = I_{N^2} \otimes (\mathbf{K}_1^{\dagger} \mathbf{K}_1) + I_N \otimes (\mathbf{K}_2^{\dagger} \mathbf{K}_2) \otimes I_N + (\mathbf{K}_3^{\dagger} \mathbf{K}_3) \otimes I_{N^2}$ is then presented by

$$\left\{ \mu_{j_1}^{(1)} + \mu_{j_2}^{(2)} + \mu_{j_3}^{(3)} : 1 \le j_1, j_2, j_3 \le N \right\}. \tag{2.22}$$

We then aim to find the minimum of $\mu_j^{(i)}$, which is $\min\{\mu_{N-1}^{(i)}, \mu_N^{(i)}\}$. We define $f(x) = \arctan(\frac{4x}{4-x^2})$, where $x = \mathbf{k}_i h$ is such that |x| < 1 due to the condition (2.20). By the mean value theorem, |f(x)| = |f(x) - f(0)| = |f'(c)x| for some c strictly between 0 and x. Since $f'(c) = \frac{4}{4+c^2} \in (0,1)$, we have $|\phi_i| = |f(x)| < |x| = |\mathbf{k}_i h|$. Thus $|\phi_i| < \pi h$ and

$$\min_{1 \le j \le N} \mu_j^{(i)} = \left(\frac{2}{h^2} + \frac{k_i^2}{2}\right) \left(1 - \max\{\cos(\phi_i), \cos(2\pi h - \phi_i)\}\right) = k_i^2.$$
 (2.23)

Here we substitute $\cos(\phi_i) = \frac{4 - k_i^2 h^2}{4 + k_i^2 h^2}$ derived from its tangent value into the above computation. Finally, due to (2.22), the minimum eigenvalue of \mathcal{L} is $\|\mathbf{k}\|_2^2$, and thus $\lambda_1^{\mathcal{B}} = \|\mathbf{k}\|_2^2$.

Proposition 2.5. For the kernel compensation formulation (2.13) with coordinate change $\mathbf{A} = I_3$, the null space \mathcal{H} and the choice of the penalty coefficient γ are determined as follows: (1). The null space \mathcal{H} is defined by: if $\mathbf{k} = \mathbf{0}$, then

$$\mathcal{H} = \operatorname{span}\{\boldsymbol{o}_i\}_{i=1}^3, \quad \boldsymbol{o}_i \in \mathbb{R}^{3N^3}, \quad (\boldsymbol{o}_i)_j = \begin{cases} 1, & \text{if } (i-1)N^3 + 1 \le j \le iN^3, \\ 0, & \text{otherwise.} \end{cases}$$

$$(2.24)$$

If $\mathbf{k} \neq \mathbf{0}$ and condition (2.20) holds, then $\mathcal{H} = \{\mathbf{0}\}.$

(2). The following choice of γ is sufficient for the correctness of (2.13):

$$\gamma = \begin{cases} \max\{1, \lambda_m^{\mathcal{A}}\}, & \mathbf{k} = \mathbf{0}, \\ \max\{1, \lambda_m^{\mathcal{A}}\} \cdot \max\{1, \|\mathbf{k}\|_2^{-2}\}, & \mathbf{k} \neq \mathbf{0}. \end{cases}$$
 (2.25)

Proof. If $\mathbf{k} \neq \mathbf{0}$, Lemma 2.4 shows that \mathcal{L} is invertible, $\ker \mathcal{L} = \{0\}$. It follows that $\mathcal{H} = \ker(\mathcal{A}\mathcal{A}^{\dagger} + \mathcal{B}^{\dagger}\mathcal{B}) = \{\mathbf{0}\}$. If $\mathbf{k} = \mathbf{0}$, $\mathcal{L} = \sum_{i=1}^{3} \mathcal{D}_{i}^{\dagger}\mathcal{D}_{i}$, we have $\ker \mathcal{L} = \bigcap_{i=1}^{3} \ker \mathcal{D}_{i}$ due to the positive semi-definiteness. The circulant matrix \mathbf{D}_{1} has a one-dimensional kernel spanned by the vector of all ones, $\mathbf{1}_{N}$. Due to the Kronecker product structure of the \mathcal{D}_{i} , their common

kernel is $\ker \mathcal{L} = \operatorname{span}\{\mathbf{1}_{N^3}\}$ with $\mathbf{1}_{N^3} = \mathbf{1}_N \otimes \mathbf{1}_N$. It follows that \mathcal{H} is spanned by $(\mathbf{1}_{N^3}, \mathbf{0}, \mathbf{0})^{\top}$, $(\mathbf{0}, \mathbf{1}_{N^3}, \mathbf{0})^{\top}$, and $(\mathbf{0}, \mathbf{0}, \mathbf{1}_{N^3})^{\top}$, which are the vectors $\{\boldsymbol{o}_i\}_{i=1}^3$. To ensure $\gamma \lambda_1^{\mathcal{B}} \geq \lambda_m^{\mathcal{A}}$: if $\mathbf{k} \neq \mathbf{0}$, Proposition 2.4 reveals $\lambda_1^{\mathcal{B}} = \|\mathbf{k}\|_2^2$, the choice clearly

To ensure $\gamma \lambda_1^{\mathcal{B}} \geq \lambda_m^{\mathcal{A}}$: if $\mathbf{k} \neq \mathbf{0}$, Proposition 2.4 reveals $\lambda_1^{\mathcal{B}} = \|\mathbf{k}\|_2^2$, the choice clearly satisfies the condition; if $\mathbf{k} = \mathbf{0}$, the smallest nonzero eigenvalue of $\mathbf{K}_i^{\dagger} \mathbf{K}_i$ equals $\frac{4}{h^2} \sin^2(\pi h)$. Since $\frac{\sin x}{x} > \sin 1$ within the bound $x = \pi h \in (0, 1)$, which yields that $\lambda_1^{\mathcal{B}} > 4\pi^2(\sin 1)^2$. Thus $\gamma = \max\{1, \lambda_m^{\mathcal{A}}\}$ is sufficient.

Remark 2.6. Condition (2.20) is reasonable: $|\mathbf{k}_i| \leq \pi$ is satisfied by construction at high symmetry points, as is shown in (4.2) in Section 4; $N > \pi$ holds for any reasonable grid. Furthermore, in our numerical experiments the desired eigenvalues are such that $\lambda_m^A < 4\pi^2$ (more precisely, the normalized frequency $\sqrt{\lambda_m^A}/(2\pi) < 1$). Thus (2.25) reduces to a more practical formula, where γ is independent of the grid division N:

$$\gamma = \begin{cases} 4\pi^2, & \mathbf{k} = \mathbf{0} \text{ or } ||\mathbf{k}||_2 > 1, \\ 4\pi^2 ||\mathbf{k}||_2^{-2}, & ||\mathbf{k}||_2 \in (0, 1). \end{cases}$$
(2.26)

We also point out that, for a general coordinate change matrix \mathbf{A} , the corresponding results of Lemma 2.4 (1), Proposition 2.5 (1) still hold. Meanwhile, the choice of γ in (2.26) for $\mathbf{A} = I_3$ case is also valid for our numerical examples.

In summary, Proposition 2.5 provides a rigorous justification for our kernel compensation solver. It proves that for any nonzero \mathbf{k} , the null space \mathcal{H} is completely eliminated. When $\mathbf{k} = \mathbf{0}$, \mathcal{H} is reduced to a three-dimensional space corresponding to constant fields. Moreover, it provides a simple and effective rule (2.26) for choosing the penalty coefficient γ .

Remark 2.7. A notable advantage of our finite-difference-based formulation lies in the modest penalty required, which leads to a relatively well-conditioned system. Our analysis shows $\gamma = O(1)$ is sufficient. In contrast, kernel compensation within a finite element framework necessitates a much larger penalty, typically $O(h^{-3})$, to counteract the scaling of the mass matrix. As noted in [13], where penalty coefficient is chosen to be $\gamma = \frac{2}{h^3}$ in the experiment, spurious eigenvalues are still likely to occur.

2.4 Matrix-Free Operations and Preconditioning

In this subsection, we aim for matrix-free operation $\mathbf{H}_h \mapsto (\mathcal{A}\mathcal{M}_{\varepsilon}\mathcal{A}^{\dagger} + \gamma \mathcal{B}^{\dagger}\mathcal{B})\mathbf{H}_h$ and the approach to preconditioning the system matrix $\mathcal{A}\mathcal{M}_{\varepsilon}\mathcal{A}^{\dagger} + \gamma \mathcal{B}^{\dagger}\mathcal{B}$ effectively using the discrete Fourier transform (DFT). We define the $N^3 \times N^3$ 3D DFT matrix \mathcal{F} as the tensor product of three 1D DFT matrices:

$$\mathcal{F} = \mathbf{F} \otimes \mathbf{F} \otimes \mathbf{F}. \tag{2.27}$$

Applying the mixed product property (2.15) and Lemma 2.1, we establish the \mathcal{F} -diagonalization of matrices \mathcal{D}_i for i = 1, 2, 3.

Proposition 2.8. Assuming $\mathbf{D}_i = \mathbf{F} \Lambda_i \mathbf{F}^{\dagger}$ for i = 0, 1, where diagonal matrices Λ_i are derived

from (2.14), the matrices \mathcal{D}_i admit the factorization

$$\mathcal{D}_{i} = \mathcal{F}\mathcal{K}_{i}\mathcal{F}^{\dagger}, \quad i = 1, 2, 3, \quad \text{where } \begin{cases} \mathcal{K}_{1} = I_{N^{2}} \otimes (\Lambda_{1} + ik_{1}\Lambda_{0}), \\ \mathcal{K}_{2} = I_{N} \otimes (\Lambda_{1} + ik_{2}\Lambda_{0}) \otimes I_{N}, \\ \mathcal{K}_{3} = (\Lambda_{1} + ik_{3}\Lambda_{0}) \otimes I_{N^{2}}. \end{cases}$$

$$(2.28)$$

If we further define $\mathcal{F}_3 := \operatorname{diag}(\mathcal{F}, \mathcal{F}, \mathcal{F})$, the matrices $\mathcal{A}, \mathcal{B}^{\dagger}\mathcal{B}$ are factorized as:

$$\mathcal{A} = \mathcal{F}_{3} \mathcal{K}_{\mathcal{A}} \mathcal{F}_{3}^{\dagger}, \quad \mathcal{B}^{\dagger} \mathcal{B} = \mathcal{F}_{3} \mathcal{K}_{\mathcal{B}} \mathcal{F}_{3}^{\dagger}, \quad where$$

$$\mathcal{K}_{\mathcal{A}} = \begin{pmatrix}
-\mathcal{K}_{3} & \mathcal{K}_{2} \\
\mathcal{K}_{3} & -\mathcal{K}_{1}
\end{pmatrix}, \quad \mathcal{K}_{\mathcal{B}} = \begin{pmatrix}
\mathcal{K}_{1}^{\dagger} \\
\mathcal{K}_{2}^{\dagger} \\
\mathcal{K}_{3}^{\dagger}
\end{pmatrix} \begin{pmatrix}
\mathcal{K}_{1} & \mathcal{K}_{2} & \mathcal{K}_{3}
\end{pmatrix}.$$
(2.29)

Proof. The result follows directly from previous propositions.

Since $\mathcal{A}M_{\varepsilon}\mathcal{A}^{\dagger} + \gamma \mathcal{B}^{\dagger}\mathcal{B} = \mathcal{F}_{3}(\mathcal{K}_{\mathcal{A}}\mathcal{F}_{3}^{\dagger}M_{\varepsilon}\mathcal{F}_{3}\mathcal{K}_{\mathcal{A}}^{\dagger} + \gamma \mathcal{K}_{\mathcal{B}})\mathcal{F}_{3}^{\dagger}$, by eliminating \mathcal{F}_{3} on both sides the kernel compensation formulation (2.13) is simplified into the equivalent system:

$$(\mathcal{K}_{\mathcal{A}}\mathcal{F}_{3}^{\dagger}\mathcal{M}_{\varepsilon}\mathcal{F}_{3}\mathcal{K}_{\mathcal{A}}^{\dagger} + \gamma\mathcal{K}_{\mathcal{B}})\boldsymbol{x} = \omega_{h}^{2}\boldsymbol{x}, \quad \boldsymbol{x} = \mathcal{F}_{3}^{\dagger}\boldsymbol{H}_{h}. \tag{2.30}$$

To construct an effective preconditioner, we consider an approximation by neglecting the middle term $\mathcal{F}_3^{\dagger}\mathcal{M}_{\varepsilon}\mathcal{F}_3$. This yields the following matrix:

$$\mathcal{K}_{\mathcal{P}} := \mathcal{K}_{\mathcal{A}} \mathcal{K}_{\mathcal{A}}^{\dagger} + \gamma \mathcal{K}_{\mathcal{B}}. \tag{2.31}$$

Therefore, once we select an iterative algebraic eigensolver, a complete formulation of operations during each iteration is

$$\begin{cases}
\text{Original system:} & (\mathcal{K}_{\mathcal{A}}\mathcal{F}_{3}^{\dagger}\mathcal{M}_{\varepsilon}\mathcal{F}_{3}\mathcal{K}_{\mathcal{A}}^{\dagger} + \gamma\mathcal{K}_{\mathcal{B}})\boldsymbol{x} = \omega_{h}^{2}\boldsymbol{x}, \\
\text{Preconditioning:} & \boldsymbol{x} \mapsto \mathcal{K}_{\mathcal{P}}^{-1}\boldsymbol{x}, \quad \mathcal{K}_{\mathcal{P}} = \mathcal{K}_{\mathcal{A}}\mathcal{K}_{\mathcal{A}}^{\dagger} + \gamma\mathcal{K}_{\mathcal{B}}.
\end{cases} \tag{2.32}$$

Crucially, the matrices $\mathcal{K}_{\mathcal{A}}$ and $\mathcal{K}_{\mathcal{B}}$ are assembled using the diagonal matrices defined in (2.28) and (2.29). Since $\mathcal{K}_{\mathcal{P}}$ is a 3 × 3 block matrix where each block is diagonal, its inverse $\mathcal{K}_{\mathcal{P}}^{-1}$ can be trivially computed. Meanwhile, explicit construction of sparse matrices is unnecessary since manipulations of these \mathcal{K} -matrices are reduced to piecewise vector multiplication, which significantly enhances GPU acceleration efficiency.

Proposition 2.9. The condition number of the preconditioned system (2.32) is bounded by the condition number of the permittivity matrix $\mathcal{M}_{\varepsilon}$.

Proof. We consider the Rayleigh quotient $\rho(\cdot)$ ($\|\cdot\|_2$ is vector 2-norm):

$$\rho(\boldsymbol{x}) := \frac{\boldsymbol{x}^* \mathcal{K}_{\mathcal{A}} \hat{\mathcal{M}} \mathcal{K}_{\mathcal{A}}^{\dagger} \boldsymbol{x} + \gamma \|\mathcal{K}_{\mathcal{B}} \boldsymbol{x}\|_2^2}{\|\mathcal{K}_{\mathcal{A}}^{\dagger} \boldsymbol{x}\|_2^2 + \gamma \|\mathcal{K}_{\mathcal{B}} \boldsymbol{x}\|_2^2}, \qquad \hat{\mathcal{M}} = \mathcal{F}_3^{\dagger} \mathcal{M}_{\varepsilon} \mathcal{F}_3,$$
(2.33)

where $x \in \mathbb{C}^{3N^3}$ and superscript "*" refers to vector conjugate transpose. Since \mathcal{F}_3 is unitary, $\hat{\mathcal{M}}$ has exactly the same spectrum as $\mathcal{M}_{\varepsilon}$. The inequality

$$\lambda_{\min}(\mathcal{M}_{\varepsilon})\|\boldsymbol{y}\|_{2}^{2} \leq \boldsymbol{y}^{*}\mathcal{M}_{\varepsilon}\boldsymbol{y} \leq \lambda_{\max}(\mathcal{M}_{\varepsilon})\|\boldsymbol{y}\|_{2}^{2}$$

holds for any $\mathbf{y} \in \mathbb{C}^{3N^3}$, which implies the range of the Rayleigh quotient is bounded by the minimum and maximum eigenvalues of $\mathcal{M}_{\varepsilon}$.

Remark 2.10. We give a brief summary of Section 2: Yee's scheme approximates the model problem (1.4), (2.9) and arrives at a preliminary result (2.12). Kernel compensation formulation (2.13) eliminates the null space. Finally (2.32) provides a preconditioned formulation that allows matrix-free operations for implementing $\mathcal{A}, \mathcal{B}^{\dagger}\mathcal{B}$ and preconditioning. Formulation (2.32) is adopted for numerical experiments in Section 4.

3 Treatment of Permittivity ε

To ensure the correctness and robustness of kernel compensation formulation (2.13), $\mathcal{M}_{\varepsilon}$ is strictly required to be HPD. This section details how we construct the map $\mathbf{E}_h \mapsto \mathcal{M}_{\varepsilon} \mathbf{E}_h$. Subsection 3.1 discusses the simplest case for diagonal ε_1 . When ε_1 has nonzero off-diagonal entries, we encounter the critical issue of DoF misalignment. Subsection 3.2 explains the numerical difficulty and presents two explicit solutions. Rigorous proofs of HPD properties are provided in Subsection 3.3.

To avoid ambiguity of subscripts, we specify the notations as:

$$(\mathbf{A})_{ij}$$
: the (i,j) entry of matrix \mathbf{A} ; $(\mathbf{D})_i$: the i -th entry of diagonal matrix \mathbf{D} ; \mathcal{M}_{ij} : the (i,j) matrix block of a block matrix; (3.1) \mathbf{M}_k : the k -th diagonal block of a block diagonal matrix.

The permittivity is denoted by $\varepsilon_1 = (\varepsilon_{ij})_{1 \leq i,j \leq 3}$, where ε_{ij} 's denote the entries of ε_1 . We also introduce edge and volume indicator matrices $\mathcal{I}_{\mathcal{E}} \in \mathbb{R}^{3N^3 \times 3N^3}$, $\mathcal{I}_{\mathcal{V}} \in \mathbb{R}^{N^3 \times N^3}$ to distinguish the DoFs located within the material subdomain Ω_1 :

Matrix $\mathcal{I}_{\mathcal{E}}$ can be naturally decomposed into three $N^3 \times N^3$ diagonal blocks, where each \mathcal{I}_i corresponds to the indicator matrix for edge-DoFs aligned along the *i*-th axis.

3.1 Diagonal Cases

The construction is straightforward when the material permittivity ε_1 is a diagonal matrix, i.e. $\varepsilon_1 = \operatorname{diag}(\varepsilon_{11}, \varepsilon_{22}, \varepsilon_{33}), \ \varepsilon_{ii} > 0$. In this case the dielectric matrix $\mathcal{M}_{\varepsilon}$ is also diagonal:

$$\mathcal{M}_{\varepsilon} = \operatorname{diag}(\mathcal{M}_{11}, \mathcal{M}_{22}, \mathcal{M}_{33}), \quad \mathcal{M}_{ii} = (\varepsilon_{ii} - 1)\mathcal{I}_i + I_{N^3},$$
 (3.3)

where \mathcal{I}_i is defined in (3.2). We adopt a direct pointwise evaluation of $(\mathcal{M}_{ii})_{\beta}$. While other approaches, such as that in [14], employ a local averaging of surrounding values, our simpler treatment is sufficient to maintain the overall accuracy of the scheme.

3.2 Misalignment of DoFs

A challenge arises when ε_1 contains nonzero off-diagonal entries (e.g., $\varepsilon_{12} = \varepsilon_{21}^* \neq 0$), which couple different electric field components. The staggered nature of the grid leads to a misalignment of DoFs: The evaluation of the term for the x-component of the electric field requires the quantity $\varepsilon_{12}E_2$, while E_2 is approximated by y-edge DoFs, a direct evaluation of E_2 on any x-aligned edge is not available. This misalignment problem occurs for all off-diagonal coupling terms. We propose a trivial solution and a more physically accurate interpolation-based method to address this numerical difficulty.

3.2.1 A Trivial Solution

The simplest approach is to completely neglect the spatial mismatch on the off-diagonal blocks and consider $\mathcal{I}_1, \mathcal{I}_2, \mathcal{I}_3$ as equivalent with $\mathcal{I}_{\mathcal{V}}$. In this case we define

$$\mathcal{M}_{\text{Trivial}} := \begin{pmatrix} \mathcal{M}_{11} & \varepsilon_{12} \mathcal{I}_{\mathcal{V}} & \varepsilon_{13} \mathcal{I}_{\mathcal{V}} \\ \varepsilon_{12}^* \mathcal{I}_{\mathcal{V}} & \mathcal{M}_{22} & \varepsilon_{23} \mathcal{I}_{\mathcal{V}} \\ \varepsilon_{13}^* \mathcal{I}_{\mathcal{V}} & \varepsilon_{23}^* \mathcal{I}_{\mathcal{V}} & \mathcal{M}_{33} \end{pmatrix}. \tag{3.4}$$

Although geometrically inaccurate, this approach produces a simply structured matrix, allowing matrix-free implementations of $E_h \mapsto \mathcal{M}_{\text{Trivial}} E_h$.

3.2.2 Cross-DoF Transfer via Interpolation

A more physically faithful approach is to bridge the misalignment by interpolation. We can approximate the value of a field component at a desired location by averaging the values from its nearest neighbors on the staggered grid. We adopt the notations in (2.4): for any \boldsymbol{E}_h consisting of edge-DoFs, there holds:

$$E_{i-\frac{1}{2},j,k}^{1} = \frac{1}{4} \left(E_{i-1,j-\frac{1}{2},k}^{2} + E_{i-1,j-\frac{1}{2},k}^{2} + E_{i,j-\frac{1}{2},k}^{2} + E_{i,j+\frac{1}{2},k}^{2} \right) + O(h^{2}), \tag{3.5}$$

where $O(h^2)$ is the accuracy guaranteed by the smoothness of the original field \mathbf{E} . Due to periodicity, (3.5) has a matrix representation using \mathbf{D}_0 defined in (2.5):

$$\boldsymbol{E}_h^1 = (\mathbf{D}_0 \otimes \mathbf{D}_0^\top \otimes I_N) \boldsymbol{E}_h^2 + O(h^2). \tag{3.6}$$

Likewise, we obtain a set of cross-DoF transfer matrices $\{\mathcal{T}_{ij}\}_{1\leq i,j\leq 3}$ as follows:

$$\mathbf{E}_{h}^{i} = \mathcal{T}_{ij}\mathbf{E}_{h}^{j} + O(h^{2}), \quad \mathbf{E}_{h}^{j} = \mathcal{T}_{ij}^{\top}\mathbf{E}_{h}^{i} + O(h^{2}), \quad 1 \leq i < j \leq 3,
\mathcal{T}_{12} = \mathbf{D}_{0} \otimes \mathbf{D}_{0}^{\top} \otimes I_{N}, \quad \mathcal{T}_{13} = \mathbf{D}_{0} \otimes I_{N} \otimes \mathbf{D}_{0}^{\top}, \quad \mathcal{T}_{23} = I_{N} \otimes \mathbf{D}_{0} \otimes \mathbf{D}_{0}^{\top}.$$
(3.7)

With these transfer operators, one might think it is sufficient to simply apply the edge indicator matrices $\mathcal{I}_1, \mathcal{I}_2, \mathcal{I}_3$ afterwards. However, a naive construction of the off-diagonal block, $\varepsilon_{12}\mathcal{I}_1\mathcal{T}_{12}$ for example, would lead to a non-Hermitian $\mathcal{M}_{\varepsilon}$, as $(\varepsilon_{12}\mathcal{I}_1\mathcal{T}_{12})^{\dagger} = \varepsilon_{12}^*\mathcal{T}_{12}^{\top}\mathcal{I}_1$ does not equal the corresponding (2,1) block $\varepsilon_{12}^*\mathcal{I}_2\mathcal{T}_{12}^{\top}$. To ensure Hermiticity, we construct symmetrized cross-DoF transfer operators and formulate the matrix as:

$$\mathcal{M}_{\text{CrossDoF}} := \begin{pmatrix} \mathcal{M}_{11} & \varepsilon_{12} \mathcal{S}_{12} & \varepsilon_{13} \mathcal{S}_{13} \\ \varepsilon_{12}^* \mathcal{S}_{12}^\top & \mathcal{M}_{22} & \varepsilon_{23} \mathcal{S}_{23} \\ \varepsilon_{13}^* \mathcal{S}_{13}^\top & \varepsilon_{23}^* \mathcal{S}_{23}^\top & \mathcal{M}_{33} \end{pmatrix}, \quad \mathcal{S}_{ij} = \frac{\mathcal{I}_i \mathcal{T}_{ij} + \mathcal{T}_{ij} \mathcal{I}_j}{2}, \quad 1 \le i < j \le 3.$$
 (3.8)

In practice, $\mathcal{M}_{\text{CrossDoF}}$ is explicitly assembled as a sparse matrix due to its relatively complicated structure. Although this solution consumes slightly more storage, the efficiency is barely affected, as is shown in the experiments.

3.3 Proof of HPD Property

We provide analysis for the HPD properties of the discrete permittivity matrix $\mathcal{M}_{\text{Trivial}}$ and $\mathcal{M}_{\text{CrossDoF}}$, which are expected to be HPD whenever the 3 × 3 matrix ε_1 is HPD. Unfortunately, the HPD property may not be preserved without the following assumptions:

Assumption 3.1. Eigenvalues of ε_1 lie in (0,1].

Assumption 3.2. Matrix ε_1 is strictly diagonally dominant (SDD): $\varepsilon_{ii} > \sum_{j \neq i} |\varepsilon_{ij}|, i = 1, 2, 3.$

Assumption 3.3. At least one off-diagonal entry of ε_1 is zero.

The above assumptions are reasonable in physics. The 3×3 matrix ε_1 represents the inverse of the normalized permittivity tensor ε within the material domain Ω_1 . For any physical material, ε must have eigenvalues no less than 1, with 1 corresponding to the vacuum. Consequently, the spectrum of ε_1 must lie in (0,1], as is illustrated by Assumption 3.1. In pseudochiral media, off-diagonal entries in ε_1 often arise from a rotation of the material's principal axes. A common case involves a material with anisotropy rotated only in the xy-plane, which leads to $\varepsilon_{13} = \varepsilon_{23} = 0$. Assumption 3.3 is thus satisfied in this case. Assumption 3.2 is also reasonable since many anisotropic materials exhibit strong diagonal dominance.

In Subsubsection 3.3.1 we prove that $\mathcal{M}_{\text{Trivial}}$ is HPD under Assumption 3.1 alone; Subsubsection 3.3.2 proves that $\mathcal{M}_{\text{CrossDoF}}$ is HPD if Assumption 3.1 is combined with either Assumption 3.2 or 3.3.

3.3.1 Positive Definiteness for Matrix $\mathcal{M}_{Trivial}$

In the proofs that follow, we adhere to the notations displayed in (3.1).

Lemma 3.4. For any matrix $A \in \mathbb{C}^{N \times N}$ and permutation σ over $\{1, \dots, N\}$, if matrix \hat{A} satisfies $(\hat{A})_{ij} = (A)_{\sigma(i),\sigma(j)}$, then $\hat{A} = PAP^{\top}$ where permutation matrix P is such that $(P)_{ij} = \delta_{\sigma(i),j}$ (δ is the Kronecker delta).

Proof. We have
$$(PA)_{ij} = \sum_{k=1}^{N} (P)_{ik}(A)_{kj} = (A)_{\sigma(i),j}$$
 and $(\hat{A}P)_{ij} = \sum_{k=1}^{N} (\hat{A})_{ik}(P)_{kj} = (\hat{A})_{i,\sigma^{-1}(j)}$, thus $(PA)_{ij} = (\hat{A}P)_{ij}$ holds for any $1 \le i, j \le N$.

Lemma 3.5. Let \mathcal{M} be an $mN \times mN$ Hermitian block matrix partitioned into $m \times m$ blocks $\mathcal{M} = (\mathbf{M}_{ij})_{1 \leq i,j \leq m}$, each block \mathbf{M}_{ij} is $N \times N$ diagonal and $\mathbf{M}_{ji} = \mathbf{M}_{ij}^{\dagger}$. Then there holds:

$$\lambda(\mathcal{M}) = \bigcup_{k=1}^{N} \lambda(\hat{\mathbf{M}}_k), \quad \text{where } \hat{\mathbf{M}}_k \in \mathbb{C}^{m \times m}, \ (\hat{\mathbf{M}}_k)_{ij} = (\mathbf{M}_{ij})_k. \tag{3.9}$$

Proof. We introduce matrix $\hat{\mathcal{M}}$ such that $(\hat{\mathcal{M}})_{ij} = (\mathcal{M})_{\sigma(i),\sigma(j)}$, where σ is a permutation over $\{1,\cdots,mN\}$ defined by:

$$\sigma(i) = (i - (k-1)m - 1)N + k, \quad (k-1)m + 1 \le i \le km, \quad k = 1, \dots, N.$$
(3.10)

According to the diagonal condition, $(\mathcal{M})_{ij} \neq 0$ if and only if $i \equiv j \mod N$, therefore $(\hat{\mathcal{M}})_{ij} \neq 0$ if and only if $\sigma(i) \equiv \sigma(j) \mod N$, which means i, j lay in the same interval [(k-1)m+1, km], which is equivalent to saying

$$\hat{\mathcal{M}} = \operatorname{diag}(\hat{\mathbf{M}}_1, \cdots, \hat{\mathbf{M}}_N), \quad \hat{\mathbf{M}}_k \in \mathbb{C}^{m \times m}.$$
 (3.11)

Meanwhile, $(\hat{\mathbf{M}}_k)_{ij} = (\hat{\mathcal{M}})_{(k-1)m+i,(k-1)m+j} = (\mathcal{M})_{(i-1)N+k,(j-1)N+k} = (\mathbf{M}_{ij})_k$, also $(\hat{\mathbf{M}}_k)_{ji} = (\mathbf{M}_{ji})_k = (\mathbf{M}_{ij})_k = (\hat{\mathbf{M}}_k)_{ij}^{\dagger}$, thus $\hat{\mathbf{M}}_k$ is also Hermitian. Finally, according to Lemma 3.4, \mathcal{M} shares exactly same eigenvalues with $\hat{\mathcal{M}}$, thus the desired result holds.

Proposition 3.6. The matrix $\mathcal{M}_{\varepsilon}$ defined by (3.4) in Subsubsection 3.2.1 satisfies

$$\lambda_{\min}(\mathcal{M}_{\varepsilon}) \ge \lambda_{\min}(\hat{\varepsilon}_1),\tag{3.12}$$

where

$$\hat{\varepsilon}_1 := \begin{pmatrix} \hat{\varepsilon}_{11} & \varepsilon_{12} & \varepsilon_{13} \\ \varepsilon_{12}^* & \hat{\varepsilon}_{22} & \varepsilon_{23} \\ \varepsilon_{13}^* & \varepsilon_{23}^* & \hat{\varepsilon}_{33} \end{pmatrix}, \quad \hat{\varepsilon}_{ii} = \min\{\varepsilon_{ii}, 1\}.$$

$$(3.13)$$

Proof. Due to Lemma 3.5, we have $\lambda_{\min}(\mathcal{M}_{\varepsilon}) = \min_{1 \leq k \leq N} \lambda_{\min}(\mathbf{M}_k)$, where

$$\mathbf{M}_{k} = \begin{pmatrix} (\varepsilon_{11} - 1)(\mathcal{I}_{1})_{k} + 1 & \varepsilon_{12}(\mathcal{I}_{\mathcal{V}})_{k} & \varepsilon_{13}(\mathcal{I}_{\mathcal{V}})_{k} \\ \varepsilon_{12}^{*}(\mathcal{I}_{\mathcal{V}})_{k} & (\varepsilon_{22} - 1)(\mathcal{I}_{2})_{k} + 1 & \varepsilon_{23}(\mathcal{I}_{\mathcal{V}})_{k} \\ \varepsilon_{13}^{*}(\mathcal{I}_{\mathcal{V}})_{k} & \varepsilon_{23}^{*}(\mathcal{I}_{\mathcal{V}})_{k} & (\varepsilon_{33} - 1)(\mathcal{I}_{3})_{k} + 1 \end{pmatrix}.$$
(3.14)

When $(\mathcal{I}_{\mathcal{V}})_k = 0$, \mathbf{M}_k is diagonal with positive entries; when $(\mathcal{I}_{\mathcal{V}})_k = 1$, $\mathbf{M}_k \geq \hat{\varepsilon}_1$. Therefore $\lambda_{\min}(\mathcal{M}_{\varepsilon}) \geq \min\{\lambda_{\min}(\hat{\varepsilon}_1), \hat{\varepsilon}_{11}, \hat{\varepsilon}_{22}, \hat{\varepsilon}_{33}\}$. Moreover, $\hat{\varepsilon}_{ii} = \mathbf{e}_i^{\top} \hat{\varepsilon}_1 \mathbf{e}_i \geq \lambda_{\min}(\hat{\varepsilon}_1)$ due to minimality of Rayleigh quotient, we have $\lambda_{\min}(\mathcal{M}_{\varepsilon}) \geq \lambda_{\min}(\hat{\varepsilon}_1)$.

Proposition 3.6 proves that Assumption 3.1 is sufficient for $\mathcal{M}_{Trivial}$ to be HPD.

3.3.2 Positive Definiteness for Matrix $\mathcal{M}_{\text{CrossDoF}}$

We start by considering S_{ij} 's matrix norms, which can help prove the HPD property under the SDD condition of Assumption 3.2.

Proposition 3.7. The matrices $\{S_{ij}\}_{1 \le i \le j \le 3}$ defined in (3.8) satisfies:

$$\|S_{ij}\|_1 \le 1, \quad \|S_{ij}\|_2 \le 1, \quad \|S_{ij}\|_{\infty} \le 1.$$
 (3.15)

Here $\|\cdot\|_1, \|\cdot\|_2, \|\cdot\|_\infty$ refer to the matrix column sum, spectral norm and row sum respectively.

Proof. It suffices to prove the same properties for \mathbf{D}_0 . $\|\mathbf{D}_0\|_1 = \|\mathbf{D}_0\|_{\infty} = 1$ is trivial due to (2.6). By Lemma (2.1), it is known that $\|\mathbf{D}_0\|_2 = 1$. Therefore Kronecker 2-norm of products of $\mathbf{D}_0, \mathbf{D}_0^{\mathsf{T}}$ and I_N also equals 1, which implies $\|\mathcal{S}_{ij}\|_2 \leq 1$. Next we verify that $\|A \otimes B\|_{\infty} = \|A\|_{\infty} \|B\|_{\infty}$ for any matrix A, B. If this holds, then $\|\mathcal{S}_{ij}\|_{\infty} \leq 1$ holds. Also $\|A \otimes B\|_1 = \|A^{\mathsf{T}} \otimes B^{\mathsf{T}}\|_{\infty} = \|A^{\mathsf{T}}\|_{\infty} \|B^{\mathsf{T}}\|_{\infty} = \|A\|_1 \|B\|_1$, which implies $\|\mathcal{S}_{ij}\|_1 \leq 1$.

For simplicity we assume $A=(a_{ij}), B=(b_{st}) \in \mathbb{R}^{N \times N}$. Since $(A \otimes B)_{I,J}=a_{ij}b_{st}$, where I=(i-1)N+s, J=(j-1)N+t, thus

$$||A \otimes B||_{\infty} = \max_{I} \sum_{J} |(A \otimes B)_{I,J}| = \max_{i,s} \sum_{j,t}^{N} |a_{ij}b_{st}| = \max_{i} \sum_{j} |a_{ij}| \max_{s} \sum_{t} |b_{st}| = ||A||_{\infty} ||B||_{\infty},$$

where I, J vary from 1 to N^2 and i, j, s, t vary from 1 to N. The proof is completed.

Proposition 3.8. If Assumptions 3.1 and 3.2 hold, then $\mathcal{M}_{CrossDoF}$ is SDD. Hence $\mathcal{M}_{CrossDoF}$ is HPD according to Gerschogrin's theorem.

Proof. $\mathcal{M}_{\text{CrossDoF}}$ being SDD is a straightforward result from $\|\mathcal{S}_{ij}\|_1, \|\mathcal{S}_{ij}\|_{\infty} \leq 1$ by shrinking the diagonal blocks \mathcal{M}_{ii} to $\varepsilon_{ii}I_{N^3}$.

Next we prove a general conclusion in verifying positive-definiteness of Hermitian block matrix to verify the sufficiency of Assumption 3.3, as is illustrated in the following lemma:

Lemma 3.9. We assume a set of m^2 matrices $\{S_{ij}\}_{1 \leq i < j \leq m}$, where $S_{ij} \in \mathbb{C}^{N \times N}$, to satisfy: $S_{ii} = I_N$ for $i = 1, \dots, N$ and $S_{ji} = S_{ij}^{\dagger}$, $\|S_{ij}\|_2 \leq 1$ for $1 \leq i < j \leq N$. We define $mN \times mN$ block matrix M with blocks $M := \{\varepsilon_{ij}S_{ij}\}_{1 \leq i,j \leq m}$, where (ε_{ij}) forms an $m \times m$ HPD matrix. If ε is tridiagonal, then M is HPD.

Proof. For any $z_1, \dots, z_m \in \mathbb{C}$, we denote $z_i = a_i \exp(i\theta_i)$ with $a_i = |z_i|$ and $\theta_i = \arg z_i$. Then

$$0 < (z_1^*, \dots, z_m^*) \varepsilon \begin{pmatrix} z_1 \\ \vdots \\ z_m \end{pmatrix} = \sum_{i=1}^m \varepsilon_{ii} a_i^2 + 2 \sum_{i=1}^{m-1} \operatorname{Re}(\varepsilon_{i,i+1} z_i^* z_{i+1})$$

$$= \sum_{i=1}^m \varepsilon_{ii} a_i^2 + 2 \sum_{i=1}^{m-1} |\varepsilon_{i,i+1}| a_i a_{i+1} \cos(\theta_{i+1} - \theta_i + \arg(\varepsilon_{ij})).$$
(3.16)

By inductively setting $\theta_1 = 0$ and $\theta_{i+1} = \theta_i - \arg(\varepsilon_{i,i+1}) + \pi$, we obtain

$$\sum_{i=1}^{m} \varepsilon_{ii} a_i^2 - 2 \sum_{i=1}^{m-1} |\varepsilon_{ij}| a_i a_j > 0, \quad \forall a_1, \dots, a_m \ge 0, \ (a_1, \dots, a_m) \ne \mathbf{0}.$$
 (3.17)

Then for any $x_1, \dots, x_m \in \mathbb{C}^N$, there holds

$$(\boldsymbol{x}_{1}^{*}, \cdots, \boldsymbol{x}_{m}^{*}) \mathcal{M} \begin{pmatrix} \boldsymbol{x}_{1} \\ \vdots \\ \boldsymbol{x}_{m} \end{pmatrix} = \sum_{i=1}^{m} \varepsilon_{ii} \|\boldsymbol{x}_{i}\|^{2} + 2 \sum_{i=1}^{m-1} \operatorname{Re}(\varepsilon_{ij} \boldsymbol{x}_{i}^{*} \mathcal{S}_{i,i+1} \boldsymbol{x}_{j})$$

$$\geq \sum_{i=1}^{m} \varepsilon_{ii} \|\boldsymbol{x}_{i}\|^{2} - 2 \sum_{i=1}^{m-1} |\varepsilon_{ij}| \|\boldsymbol{x}_{i}\| \|\boldsymbol{x}_{j}\|,$$
(3.18)

where we apply the condition $\|S_{ij}\|_2 \leq 1$. Thus (3.17) implies that right-hand side of (3.18) is nonnegative and equals zero if and only if all x_i vanish.

With the help of Lemma 3.9, the sufficiency of Assumption 3.3 is apparent.

Proposition 3.10. When Assumptions 3.1 and 3.3 hold, $\mathcal{M}_{CrossDoF}$ defined by (3.8) is HPD.

Proof. If at least one off-diagonal entries of ε_1 vanish, then ε_1 is either tridiagonal or similar to a tridiagonal matrix due to Lemma 3.4. Thus by shrinking diagonal entries of $\mathcal{M}_{\varepsilon}$ to $\min\{1, \varepsilon_{ii}\} = \varepsilon_{ii}$, applying Proposition 3.7 and Lemma 3.9, we conclude that $\mathcal{M}_{\varepsilon}$ is HPD. \square

4 Numerical experiments

All calculations are carried out based on the matrix-free kernel compensation formulation (2.32) with penalty coefficient γ set by (2.26). We consider the simple cubic (SC), face-centered cubic (FCC) and body-centered cubic (BCC) lattices. The primitive lattice vectors $(\boldsymbol{a}_1, \boldsymbol{a}_2, \boldsymbol{a}_3)$ of the lattice types, which can be found in [8], are specified as:

$$\begin{cases} \text{SC lattice:} & \boldsymbol{a}_{1} = (1,0,0)^{\top}, \quad \boldsymbol{a}_{2} = (0,1,0)^{\top}, \quad \boldsymbol{a}_{3} = (0,0,1)^{\top}, \\ \text{FCC lattice:} & \boldsymbol{a}_{1} = (0,\frac{1}{2},\frac{1}{2})^{\top}, \quad \boldsymbol{a}_{2} = (\frac{1}{2},0,\frac{1}{2})^{\top}, \quad \boldsymbol{a}_{3} = (\frac{1}{2},\frac{1}{2},0)^{\top}, \\ \text{BCC lattice:} & \boldsymbol{a}_{1} = (-\frac{1}{2},\frac{1}{2},\frac{1}{2})^{\top}, \quad \boldsymbol{a}_{2} = (\frac{1}{2},-\frac{1}{2},\frac{1}{2})^{\top}, \quad \boldsymbol{a}_{3} = (\frac{1}{2},\frac{1}{2},-\frac{1}{2})^{\top}. \end{cases}$$

$$(4.1)$$

The wave number vector \mathbf{k} in model problem (1.4) is derived from symmetry points and partition points on their connecting lines in the Brillouin zone. These Symmetry points are:

$$\begin{cases} \text{SC:} & \Gamma(0,0,0), L(\pi,0,0), M(\pi,\pi,0), N(\pi,\pi,\pi), \\ \text{FCC:} & X(0,2\pi,0), U(\frac{\pi}{2},2\pi,\pi), L(\pi,\pi,\pi), \Gamma(0,0,0), W(\pi,2\pi,0), K(\frac{3\pi}{2},\frac{3\pi}{2},0), \\ \text{BCC:} & H'(2\pi,0,0), \Gamma(0,0,0), P(\pi,\pi,\pi), N(\pi,0,\pi), H(0,2\pi,0). \end{cases}$$
(4.2)

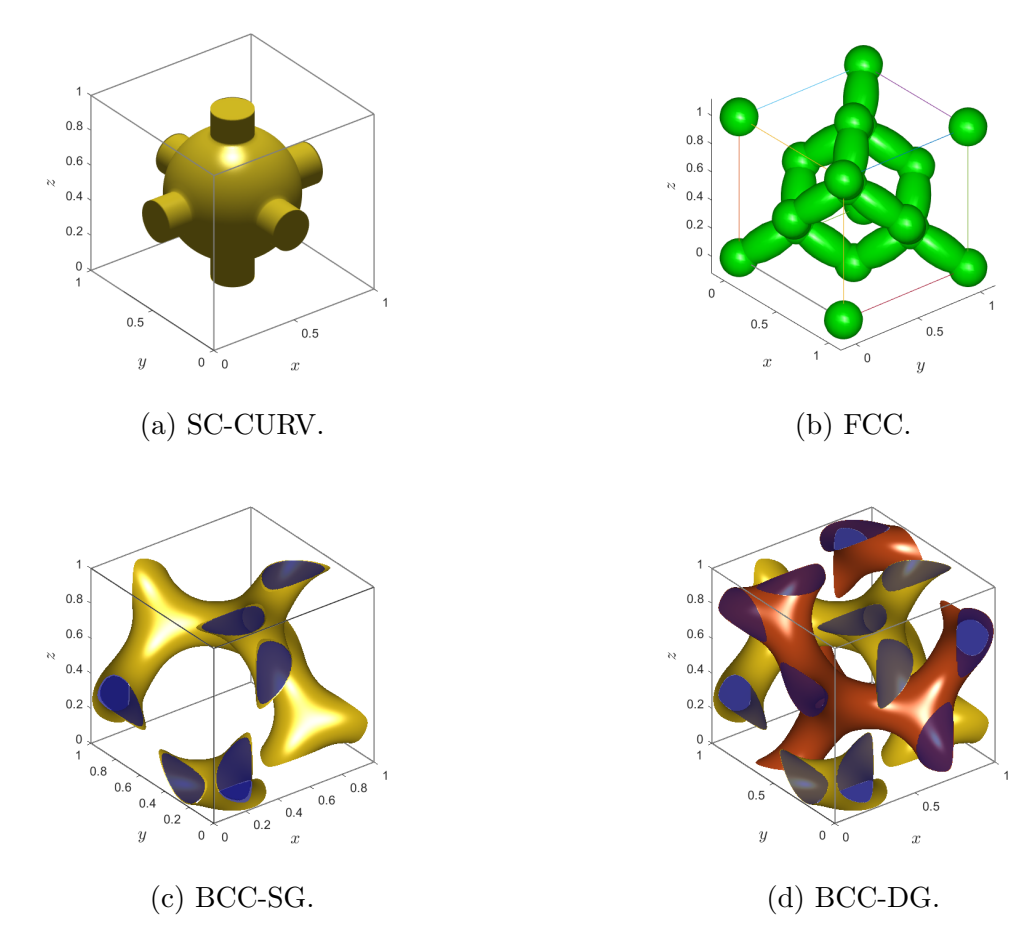


Figure 2: Figures of material structures of four sample lattices in cubic domain [0, 1]³.

The primitive lattice vectors (4.1) and symmetry points (4.2) are given in dimensionless units, which corresponds to setting the lattice constant to unity. This choice is independent of any physical scaling and is made without loss of generality, as such a scaling constant does not affect the results or efficiency. We investigate four distinct lattice structures, the unit cells of which are visually presented in Figure 2. These models can be found in [5, 11, 15].

For simplicity, we will refer to these structures by abbreviations:

- SC-CURV (SC lattice with curved surface): The SC lattice shown in Figure 2a is composed of a sphere with radius 0.345 and four cylinders with base radius 0.11.
- FCC: The FCC lattice in Figure 2b adopts a diamond structure. Its material configuration is sp^3 -like, consisting of spheres with radius of 0.12 and connecting spheroids of minor axis 0.11. The foci of the spheroids are located at the centers of the spheres.
- BCC-SG (BCC lattice with single gyroid surface): The BCC lattice in Figure 2c has its material domain specified by $\{x \in \Omega : g(x) > 1.1\}$, where

$$g(x,y,z) = \sin(2\pi x)\cos(2\pi y) + \sin(2\pi y)\cos(2\pi z) + \sin(2\pi z)\cos(2\pi x).$$

• BCC-DG (BCC lattice with double gyroid surface): Similar to BCC-SG, the material domain of BCC lattice shown in Figure 2d is specified by $\{x \in \Omega : |g(x)| > 1.1\}$.

The matrix eigenproblem (2.32) is solved by a custom-implemented LOBPCG (Locally Optimal Block Preconditioned Conjugate Gradient) solver with soft locking [9] in Python. We define the relative residual for the j-th eigenvalue-eigenvector pair $(\omega_{h,i}^2, x_j)$ as

$$\operatorname{Res}_{j} := \frac{\left\| (\mathcal{A} \mathcal{M}_{\varepsilon} \mathcal{A}^{\dagger} + \gamma \mathcal{B}^{\dagger} \mathcal{B}) \boldsymbol{x}_{j} - \omega_{h,j}^{2} \boldsymbol{x}_{j} \right\|_{2}}{\left\| \boldsymbol{x}_{j} \right\|_{2}}, \quad \left\| \cdot \right\|_{2} \text{ refers to the 2-norm.}$$

$$(4.3)$$

Convergence is considered to be reached when $\operatorname{Res}_i \leq 10^{-5}$ for all desired eigenpairs.

This section is outlined as: In Subsection 4.1, we plot the band structures and analyze the differences adopting $\mathcal{M}_{Trivial}$ and $\mathcal{M}_{CrossDoF}$. In Subsection 4.2 the iteration count, runtime and speedup by GPU acceleration efficiency are recorded and analyzed. Finally we simulate extreme cases to demonstrate the robustness of our scheme in Subsection 4.3. All programs are implemented on a platform equipped with NVIDIA GeForce RTX 4090 D GPUs, 24 GiB of memory, utilizing CUDA Version 12.4 and Driver Version 550.144.03 for GPU acceleration. The source code has been made publicly available on GitHub https://github.com/Epsilon-79th/linear-eigenvalue-problems-in-photonic-crystals.

4.1 Band Structures of isotropic and Pseudochiral Systems

The expression of ε_1 , which refers to the inverse of permittivity inside Ω_1 as we define in (1.5), is chosen to be

$$\varepsilon_{1} = \varepsilon_{\text{lattice}}^{-1} I_{3}, \quad \text{for isotropic systems,}$$

$$\varepsilon_{1} = \varepsilon_{\text{lattice}}^{-1} \begin{pmatrix} \sqrt{1 + |\beta|^{2}} & -|\beta| i \\ |\beta| i & \sqrt{1 + |\beta|^{2}} \\ 1 \end{pmatrix}, \quad \text{for pseudochiral systems;}$$

$$(4.4)$$

where the external magnetic field intensity $\beta = 0.875$, $\varepsilon_{\text{lattice}}$ is a constant depending on the type of lattice. We set $\varepsilon_{\text{lattice}} = 13$ for the SC and FCC lattice and $\varepsilon_{\text{lattice}} = 16$ for the BCC lattice. We compute the first 10 smallest frequencies with grid division N = 120 and discrete permittivity matrix $\mathcal{M}_{\varepsilon} = \mathcal{M}_{\text{CrossDoF}}$. The band structures are presented in Figures 3–6, where first 10 eigenpairs are computed for each material. Bandgap is an interval where no frequency exists, as is highlighted in yellow in the figures. The ratio of the bandgap is defined by

gap ratio :=
$$\frac{\omega_{\rm up} - \omega_{\rm low}}{(\omega_{\rm up} + \omega_{\rm low})/2}$$
, (4.5)

where $\omega_{\rm up}$ is the minimum frequency above the bandgap while $\omega_{\rm low}$ is the maximum frequency below the bandgap. The values of gap ratio of different PCs are marked in the title, as is shown in Figures 3–6. It can be observed that the gap ratios of SC-CURV, FCC and BCC-SG shrink with the presence of off-diagonal term $\varepsilon_{12} = -|\beta|i$. For BCC-DG, the existence of Weyl points shown in Figure 6 coincides with the results in [11].

We also compute complete band structures of the above models with $\mathcal{M}_{\varepsilon} = \mathcal{M}_{Trivial}$. It is

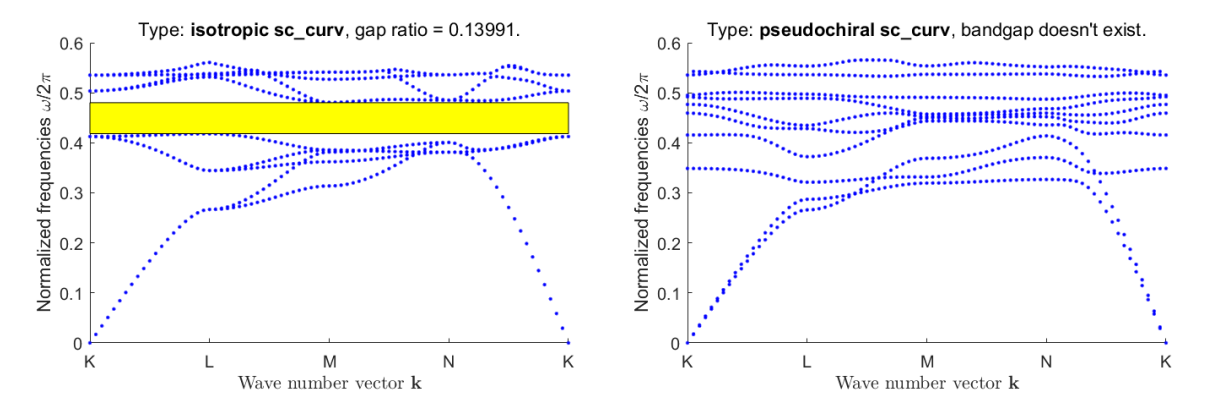


Figure 3: Band structures of SC lattice with curved material interface. Left: isotropic system; Right: pseudochiral system. Grid division N=120.

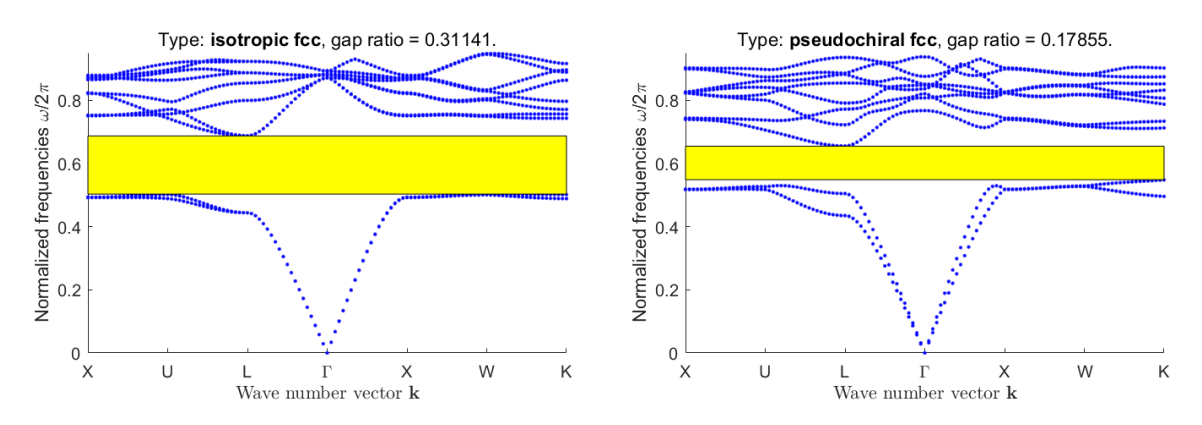


Figure 4: Band structures of FCC lattice. Left: isotropic system; Right: pseudochiral system. Grid division N=120.

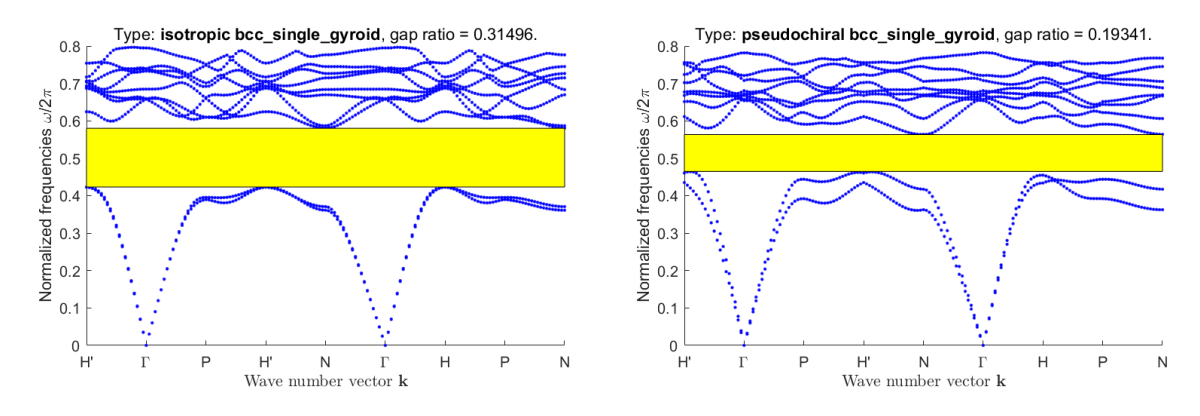


Figure 5: Band structures of BCC lattice with single gyroid surfaces. Left: isotropic system; Right: pseudochiral system. Grid division N=120.

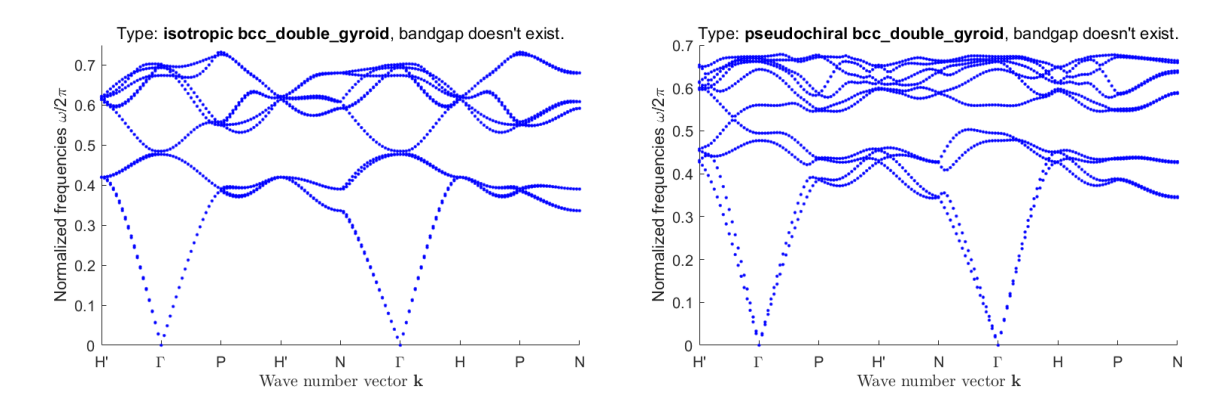


Figure 6: Band structures of BCC lattice with double gyroid surfaces. Left: isotropic system; Right: pseudochiral system. Grid division N = 120.

hard to perceive the difference directly if both band structures are plotted on the same figure. Instead we present their numerical difference in Table 1. The maximum and mean relative difference $\Delta\omega_{\rm max}$, $\Delta\omega_{\rm mean}$ are defined by

$$\Delta\omega_{\max} = \max_{\mathbf{k},j} \left\{ \frac{|\omega_{h,j}^{(1)}(\mathbf{k}) - \omega_{h,j}^{(2)}(\mathbf{k})|}{|\omega_{h,j}^{(2)}(\mathbf{k})|} \right\}, \quad \Delta\omega_{\text{mean}} = \max_{\mathbf{k},j} \left\{ \frac{|\omega_{h,j}^{(1)}(\mathbf{k}) - \omega_{h,j}^{(2)}(\mathbf{k})|}{|\omega_{h,j}^{(2)}(\mathbf{k})|} \right\}, \quad (4.6)$$

where $\omega_{h,j}^{(1)}(\mathbf{k}), \omega_{h,j}^{(2)}(\mathbf{k})$ denote the j-th frequency at the wave number vector \mathbf{k} and grid size h. The superscripts (1), (2) correspond to permittivity matrix $\mathcal{M}_{\text{Trivial}}$ and $\mathcal{M}_{\text{CrossDoF}}$, respectively. As is shown in Table 1, the difference is rather minor.

Table 1: Maximum and mean relative difference of frequencies computed with two types of $\mathcal{M}_{\varepsilon}$ in Subsection 4.1 over the complete band.

Lattice type	SC-CURV	FCC	BCC-SG	BCC-DG
$\Delta\omega_{ m max}$	2.93×10^{-3}	2.76×10^{-3}	4.71×10^{-3}	4.72×10^{-3}
$\Delta\omega_{\mathrm{mean}}$	9.88×10^{-4}	1.08×10^{-3}	1.47×10^{-3}	1.08×10^{-3}

4.2 Computational Performance

In Table 2 we present iteration counts required to achieve convergence for the types of PCs discussed in Subsection 4.1. To be precise, we compute both the average and the standard deviation of iterations at different \mathbf{k} 's, showing the numbers don't vary too much.

More iterations are required when computing pseudochiral system than that of computing isotropic system with same lattice type and tolerance. Specifically, $\mathcal{M}_{\varepsilon} = \mathcal{M}_{\text{CrossDoF}}$ requires fewer iterations than $\mathcal{M}_{\varepsilon} = \mathcal{M}_{\text{Trivial}}$.

We also provide an convergence performance where an average convergence order of relative error is estimated, as is shown in Table 3. An approximate second order convergence of the first three frequencies of the pseudochiral FCC lattice at $\mathbf{k} = (\pi, \pi, \pi)$ can be witnessed.

Table 2: Average iterations (and standard deviation) for computing complete band structure. Grid division N = 120, first 10 eigenpairs are computed with tolerance 10^{-5} .

	SC-CURV	FCC	BCC-SG	BCC-DG
Isotropic	32.8(4.0)	42.2 (6.9)	55.0 (6.9)	58.0 (6.6)
Pseudochiral $\mathcal{M}_{\varepsilon} = \mathcal{M}_{\text{Trivial}}$	52.3 (5.1)	54.0 (7.4)	68.7 (8.7)	76.5 (8.5)
Pseudochiral $\mathcal{M}_{\varepsilon} = \mathcal{M}_{\text{CrossDoF}}$	45.3 (4.2)	51.3 (7.9)	65.8 (8.8)	74.7 (8.1)

Table 3: Convergence analysis for the first three eigenvalues of the pseudochiral FCC lattice at $\mathbf{k} = (\pi, \pi, \pi)$, computed by $\mathcal{M}_{\varepsilon} = \mathcal{M}_{\text{CrossDoF}}$.

Eigenvalue	Absolute	Average		
Index	h = 1/16	h = 1/32	h = 1/64	Order
1	3.28e-02	8.49e-03	2.38e-03	1.89
2	3.56e-02	9.133e-03	3.28e-03	1.72
3	4.03e-02	1.41e-02	5.13e-03	1.49

Next, we provide a quantitative measure of performance enhancement brought by GPU acceleration. The linear algebra operations are done by numpy and cupy packages on CPU and GPU, respectively. From Table 4, we observe that GPU acceleration achieves an average speedup of over 40 times.

4.3 Robustness under Extreme Cases

We construct an ill-conditioned ε_1 as $\varepsilon_1 = U \operatorname{diag}(10^{-1}, 10^{-3}, 10^{-5})U^{\dagger}$, where U is a randomly generated unitary matrix. Under the setting of SC-CURV lattice, the system is computed with both $\mathcal{M}_{\varepsilon} = \mathcal{M}_{\operatorname{Trivial}}$ and $\mathcal{M}_{\varepsilon} = \mathcal{M}_{\operatorname{CrossDoF}}$. The approximate asymptotic damping factor $\theta \in (0,1)$ is introduced to quantify the convergence rate, which is evaluated by applying linear regression to the logarithms of residuals. The dampening history of the residuals is documented in Figure 7, where we observe a smooth convergence. Moreover, $\mathcal{M}_{\operatorname{CrossDoF}}$ has better numerical performance in avoiding stagnation under extreme cases.

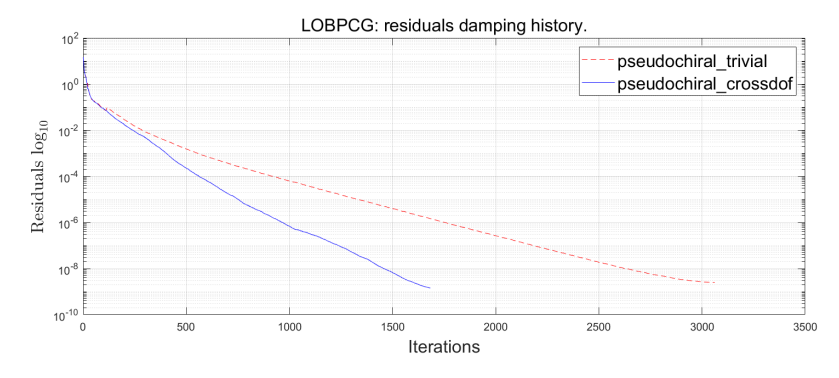


Figure 7: Convergence history where ε_1 is very ill-conditioned. Pseudochiral SC-CURV lattice at $\mathbf{k} = (\frac{1}{7}, \frac{3}{5}, \frac{4}{13})\pi$, grid division N = 120.

Table 4: CPU and GPU runtime (seconds) for the first 10 eigenvalues of SC-CURV, FCC, BCC-SG, BCC-DG at wave number vector $\mathbf{k} = (\pi, \pi, \pi)$, grid division N = 100, 120.

DoFs	Isotropic SC-CURV			Pseudochiral SC-CURV				
Dons	Steps	GPU time	CPU time	Speed up	Steps	GPU time	CPU time	Speed up
3×100^3	31	10.79	432.71	40.10	50	16.67	666.39	39.98
3×120^{3}	34	19.85	835.91	42.11	49	28.67	1297.50	45.26
DoFs	Isotropic FCC			Pseudochiral FCC				
Dons	Steps	GPU time	CPU time	Speed up	Steps	GPU time	CPU time	Speed up
3×100^{3}	45	16.00	623.77	39.01	56	19.59	852.17	43.50
3×120^{3}	45	27.71	1197.90	43.23	55	34.15	1506.35	44.11
DoFs	Isotropic BCC-SG			Pseudochiral BCC-SG				
Dors	Steps	GPU time	CPU time	Speed up	Steps	GPU time	CPU time	Speed up
3×100^{3}	57	19.85	835.33	42.08	68	24.14	1020.15	42.26
3×120^3	47	27.96	1295.39	46.33	65	41.08	1816.56	44.22
DoFs	Isotropic BCC-DG			Pseudochiral BCC-DG				
	Steps	GPU time	CPU time	Speed up	Steps	GPU time	CPU time	Speed up
3×100^3	89	26.83	1056.57	39.98	77	25.25	1038.00	41.11
3×120^3	86	44.61	1903.39	43.20	76	43.55	1971.94	45.28

5 Conclusions

In this paper, we have presented a robust, GPU-accelerated framework for solving 3D Maxwell eigenproblems in photonic crystals with pseudochiral media. Our key innovations include a novel, provably positive definite discretization for the anisotropic permittivity tensor and a rigorous completion of the kernel compensation theory, which now includes a precise characterization of the null space \mathcal{H} , an explicit rule for selecting the penalty coefficient γ , and an approach to matrix-free operations via 3D DFT for high efficiency. Numerical experiments on various lattice structures demonstrate practicality and efficiency, where an average speedup of more than $40\times$ is achieved on GPU. An ill-conditioned example also shows the robustness. Our future work will focus on extending this powerful framework to more complex, nonlinear eigenvalue problems in photonic crystals.

References

- [1] M. Chen. On the solution of circulant linear systems. SIAM J. Numer. Anal., 24:668–683, 1987.
- [2] S.-H. Chou, T.-M. Huang, T. Li, J.-W. Lin, and W.-W. Lin. A finite element based fast eigensolver for three dimensional anisotropic photonic crystals. *J. Comput. Phys.*, 386:611–631, 2019.
- [3] D. C. Dobson. An efficient method for band structure calculations in 2d photonic crystals. J. Comput. Phys., 149(2):363–376, 1999.

- [4] K. M. Ho, C. T. Chan, and C. M. Soukoulis. Existence of a photonic gap in periodic dielectric structures. *Phys. Rev. Lett.*, 65:3152–3155, Dec 1990.
- [5] T.-M. Huang, H.-E. Hsieh, W.-W. Lin, and W. Wang. Eigendecomposition of the discrete double-curl operator with application to fast eigensolver for three-dimensional photonic crystals. SIAM J. Matrix Anal. Appl., 34(2):369–391, 2013.
- [6] Y.-L. Huang, T.-M. Huang, W.-W. Lin, and W.-C. Wang. A null space free Jacobi-Davidson iteration for Maxwell's operator. SIAM J. Sci. Comput., 37(1):a1-a29, 2015.
- [7] C. Jin, Y. Xia, and Y. Xu. Kernel compensation method for Maxwell eigenproblem in photonic crystals with mimetic finite difference discretizations. *Numer. Methods Partial Differ. Equations*, 41(2):16, 2025. Id/No e23171.
- [8] J. D. Joannopoulos, S. G. Johnson, J. N. Winn, and R. D. Meade. *Photonic Crystals: Molding the Flow of Light (Second Edition)*. Princeton University Press, 2 edition, 2008.
- [9] A. V. Knyazev. Toward the optimal preconditioned eigensolver: Locally optimal block preconditioned conjugate gradient method. SIAM J. Sci. Comput., 23(2):517–541, 2001.
- [10] K. Lipnikov, G. Manzini, and M. Shashkov. Mimetic finite difference method. J. Comput. Phys., 257:1163–1227, 2014.
- [11] L. Lu, L. Fu, J. D. Joannopoulos, and M. Soljačić. Weyl points and line nodes in gyroid photonic crystals. *Nature photonics*, 7(4):294–299, 2013.
- [12] Z. Lu, A. Cesmelioglu, J. J. W. Van der Vegt, and Y. Xu. Discontinuous Galerkin approximations for computing electromagnetic Bloch modes in photonic crystals. *J. Sci. Comput.*, 70(2):922–964, 2017.
- [13] Z. Lu and Y. Xu. A parallel eigensolver for photonic crystals discretized by edge finite elements. J. Sci. Comput., 92(3):21, 2022. Id/No 79.
- [14] X.-L. Lyu, T. Li, T.-M. Huang, J.-W. Lin, W.-W. Lin, and S. Wang. FAME. Fast algorithms for Maxwell's equations for three-dimensional photonic crystals. ACM Trans. Math. Softw., 47(3):24, 2021. Id/No 26.
- [15] M. J. Mehl, D. Hicks, C. Toher, O. Levy, R. M. Hanson, G. Hart, and S. Curtarolo. The aflow library of crystallographic prototypes: Part 1. Computational Materials Science, 136:S1-S828, 2017.
- [16] W. C. Sailor, F. M. Mueller, and P. R. Villeneuve. Augmented-plane-wave method for photonic band-gap materials. *Phys. Rev. B*, 57:8819–8822, Apr 1998.
- [17] K. S. Yee. Numerical solution of initial boundary value problems involving Maxwell's equations in isotropic media. *IEEE Trans. Antennas Propag.*, 14(3):302–307, 1966.